#### Effect of imperfections on pseudo-bistability of viscoelastic domes

Tianzhen Liu<sup>a,b</sup>, Yuzhen Chen<sup>b</sup>, Liwu Liu<sup>c</sup>, Yanju Liu<sup>c</sup>, Jinsong Leng<sup>a,\*</sup>, Lihua Jin<sup>b,\*</sup>

- a. National Key Laboratory of Science and Technology on Advanced Composite in Special Environments, Harbin Institute of Technology, Harbin 150080, PR China
- b. Department of Mechanical and Aerospace Engineering, University of California, Los Angeles, Los Angeles,
   CA 90095, USA
- c. Department of Astronautical Science and Mechanics, Harbin Institute of Technology (HIT), No. 92 West Dazhi Street, PO Box 301, Harbin 150001, PR China

\*Correspondence: Lihua Jin. Email: lihuajin@seas.ucla.edu & Jinsong Leng, E-mail: lengjs@hit.edu.cn

#### **Abstract**

Snap-through instability of viscoelastic materials is known to generate novel behavior, featured as pseudo-bistability, i.e. the capability of a system in maintaining a deformed configuration for a certain period of time after removal of an external load, followed by snapping back to its initial configuration automatically, due to the combination of time-dependent mechanical property and geometric nonlinearity of the system. This work numerically, experimentally, and analytically examines spherical viscoelastic domes with predesigned geometric imperfections that can control the structural stability and tune the snap time, which is defined as the time that a dome remains almost stationary in the deformed configuration after the release of external forces. The results show that even an imperfection with a small magnitude can play a significant role in pseudo-bistability. An imperfection with a positive amplitude shifts a viscoelastic dome towards bistable behavior, corresponding to a longer snap time, while an imperfection with a negative amplitude shifts the dome towards monostable behavior, resulting in a shorter snap time. This work can open up new opportunities for controlling spatiotemporal behavior of structures for multi-functionalities.

Keywords: Geometric imperfections, Pseudo-bistability, Viscoelasticity, Snap-through instability, Dome

#### 1. Introduction

A snap-through instability refers to a mode of instability that can transform a structure from one metastable state to another non-adjacent stable state under certain loading [1-6]. Correspondingly, a large amount of stored elastic energy in the metastable state is released and converted to kinetic energy, resulting

in a very rapid transition. Snap-through instabilities widely exist in nature and daily life, such as in Venus flytraps [7], snap hair clips, and jumping popper toys [8, 9]. They also have various practical applications in engineering, such as energy absorption [10-14], actuation [15, 16] and morphing devices [17-19], by virtue of fast motion, energy storage and reversible deformation. A large amount of research has concentrated on snap-through instabilities in arches and domes [8, 20-23] due to the ubiquity of the instabilities in nature and engineering.

Viscoelasticity, which describes time-dependent and rate-dependent behavior of materials [24] [25], has profound influence on snap-through instabilities [2, 8, 11, 15, 23, 26-28]. In particular, some viscoelastic systems show the capability of maintaining a deformed configuration for a certain period of time after removal of the external load, followed by rapidly recovering its initial configuration automatically. This phenomenon is called pseudo-bistability or temporary bistability. The mechanism of pseudo-bistability is that the time evolution of the material property of a viscoelastic system can trigger a transition of the system from a monostable state to a bistable state [8, 15, 26, 27, 29]. In particular, pseudo-bistability is widely studied in viscoelastic arches and domes, and specifically, the decrease of the ratio of bending energy to stretching energy during relaxation is attributed to be the cause of pseudo-bistability in them.

It is well recognized that snap-through instabilities are highly sensitive to geometric imperfections [30-36]. In shell buckling, there was a long history in understanding the discrepancy between the theoretically predicted and experimentally observed critical buckling loads, and large knockdown factors have been introduced to account for the significant reduction of the buckling loads due to imperfections [32]. Lee et al. studied the effect of a dimple-like geometric imperfection on the critical buckling load of spherical elastic domes under pressure loading and accurately predicted the knockdown factors of imperfect spherical domes by shell theory [32]. Ref [35] identified local and global buckling loads for cylindrical shells subjected to axial compression with emphasis on the role of local geometric dimple imperfections. More recently, elastic thin domes with a large axisymmetric imperfection were examined by employing a shell theory with exact expressions of the middle surface strains and curvature changes, and were found to have significantly different buckling conditions and buckling modes from the perfect ones [31]. By comparing the buckling loads of shells with different types of geometric imperfections, Babcock concluded that the presence of a geometric imperfection serves as the most important factor, while the type of the imperfection plays a relatively minor role [33].

In view of the significant effect of geometric imperfections on snap-through buckling of spherical domes, we ask how the pseudo-bistability of viscoelastic domes is affected by geometric imperfections, which is, to our best knowledge, still absent. To answer this question, this paper uses a combined method of analytical modeling, finite element analysis (FEA) and experiments. Snap-through buckling of perfect and imperfect domes with systematically varied geometric imperfections are investigated using FEA.

Experimentally, imperfect domes are fabricated by casting a viscoelastic elastomer using molds with an engineered imperfection. To further understand the effect of imperfections on pseudo-bistability, we develop an analytical discrete model for viscoelastic domes, and examine the instantaneous and dynamic responses of both perfect and imperfect domes. Understanding the geometric role of imperfections will allow us to better harness and program pseudo-bistability of viscoelastic domes for applications.

#### 2. Methods

# 2.1 Finite element analysis

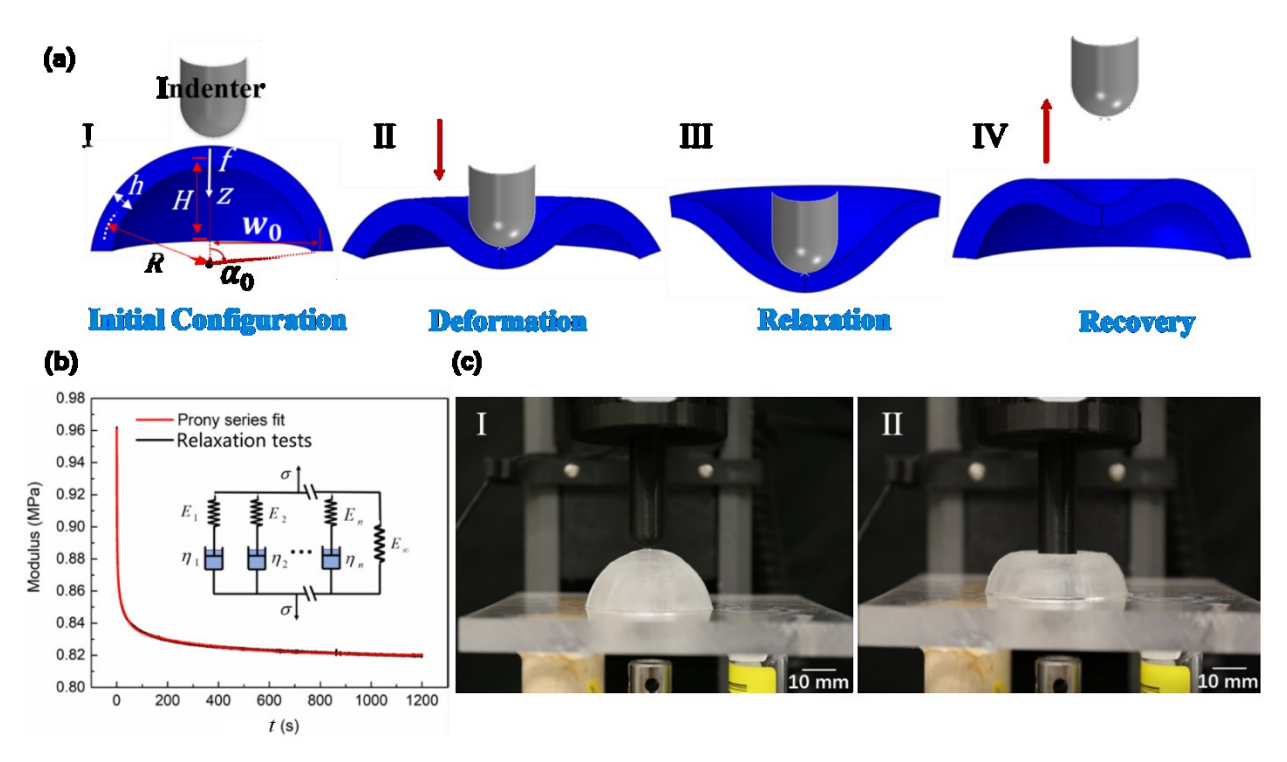


Fig.1. (a) Schematics of the loading process of a viscoelastic spherical dome under indentation in the FEA and experiments. (I) In the initial configuration the dome has an angle  $\alpha_0$  and width  $w_0$ . (II) In the deformation step, a sudden displacement is applied. (III) Then the displacement is held in the relaxation step, (IV) and finally released in the recovery step. (b) The relaxation test results for Sylgard 184 with a base-to-crosslinker ratio 15:1 fitted by the generalized Maxwell-Wiechert model. (c) The experimental silicone rubber dome and indentation testing apparatus: (I) the initial state and (II) indented state using an Instron machine with custom-mounted attachments.

The stability of perfect and imperfect viscoelastic spherical domes under a vertical indentation was investigated using FEA in Abaqus (version 6.14). The domes have an initial angle  $\alpha_0$ , width  $w_0$  and height

H (Fig.1a). The middle surface radius and thickness are denoted by R and h, respectively. Their viscoelastic behavior is modeled by the generalized Maxwell-Wiechert material, with the material parameters experimentally fitted to those of Sylgard 184 with a base-to-crosslinker ratio 15:1; see Sec 2.2 for more details. An axisymmetric rigid indenter with a ball head of a radius approximately 30% of the dome radius was used to apply a displacement to the dome, the distributed load caused by which shows advantages of eliminating the local stress concentration over a concentrated load [27]. A sudden downward displacement is applied to the apex region of the dome by the indenter from the initial configuration at t=0. (Fig.1a I) to the deformed configuration at t=0+ (Fig.1a II). The indenter is then held at the same position, and the dome relaxes under this constraint during the time period of 0- $t_{rel}$  (Fig.1a III). The base of dome is allowed to move in the horizontal plane but prohibited to have any vertical displacement (U1 is free, U2=0). Finally, the indenter was removed by deactivating the surface to surface contact between the indenter and the dome at  $t=t_{rel}$  (Fig.1a IV). The response of the viscoelastic dome under this loading process was simulated using the dynamic implicit step so that the time-dependent and quick recovery processes can be captured; numerical damping is applied with the default setting in the dynamic implicit step. Continuum axisymmetric elements (CAX4) were chosen, and the nonlinear geometry parameter NLGEOM was activated.

An axisymmetric dimple-like geometric imperfection with a positive amplitude (marked in red in Fig.2a) or a negative amplitude (marked in blue in Fig.2a) is introduced to the apex region of the perfect dome. The Abaqus INPUT files were updated using a MATLAB code for each specific profile of imperfection. The profile of the imperfection is specified by a Gaussian dimple [30],

$$W_I = \delta e^{-(\beta/\beta_I)^2} \,, \tag{1}$$

where  $\delta$  is the amplitude of the imperfection at the apex,  $\beta$  is the polar angle (Fig. 2a), and  $\beta_I$  is the exponential decay width of the imperfection.

#### 2.2 Material characterizations

Experimentally we fabricated viscoelastic domes using Sylgard 184 with a base-to-crosslinker ratio 15:1 – a silicone rubber proved to possess viscoelastic properties with Poisson's ratio of 0.469 and density of  $1030 \ kg/m^3$  [22, 37]. To determine the viscoelastic properties of the material, relaxation tests were performed on five identical thin film specimens, each with a length of 125 mm, width of 25 mm and thickness of 3 mm, using an Instron testing machine (5900 SERIES), according to the ASTM D412 standard method. In the relaxation tests, 10% strain was applied in 1 s to avoid stress relaxation during the deformation process, and maintained constant for 1200 s to allow the material to relax fully; the reaction force as a function of time was measured.

Here the generalized Maxwell-Wiechert model (Fig.1b), consisting of a free spring with a modulus  $E_{\infty}$ , and n numbers of Maxwell elements in parallel with the modulus  $E_i$  and viscosity  $\eta_i$  for the ith element, is adopted to describe the viscoelastic behavior. When a step strain  $\varepsilon = \varepsilon_0 H(t)$ , with H(t) the Heaviside step function, is applied to the model, the stress can be solved as  $\sigma(t) = \varepsilon_0 E(t)$ , where the modulus is a function of time,

$$E(t) = E_{\infty} + \sum_{i=1}^{n} E_{i} e^{-\frac{t}{\tau_{i}}}, \tau_{i} = \frac{\eta_{i}}{E_{i}},$$
 (2)

with the relaxation timescales  $\tau_i$  for the *i*th element. We can see that the modulus decreases with time from the initial value  $E_0 = E_\infty + \sum_{i=1}^n E_i$  to the long-term modulus  $E_\infty$ , which is usually non-zero for crosslinked polymers, after full relaxation. Further normalizing E(t) by the initial value  $E_0$ , we express  $g(t) = E(t)/E_0$  by a Prony series

$$g(t) = 1 - \sum_{i=1}^{n} g_i (1 - e^{-\frac{t}{\tau_i}}), \ g_i = \frac{E_i}{E_0}.$$
 (3)

It can be seen that the initial value of g(t) is 1 and the long-term value decreases to  $1 - \sum_{i=1}^{n} g_i$ , meaning the modulus relaxes by a maximum factor of  $\sum_{i=1}^{n} g_i$ . The parameters  $g_i$  and  $\tau_i$  were determined by fitting to our experimental results of the relaxation tests. The generalized Maxwell-Wiechert model reduces to the standard linear solid (SLS) model under the condition that the number of Maxwell element n=1, which will be used in the discrete model in Section 5.

The least squares approach was applied to fit the generalized Maxwell-Wiechert model with n=5 Maxwell elements to the average relaxation data of five specimens (R-Square $\geq$ 99.6%), resulting in 5 relaxation timescales ranging from 0.3s to 500s, and the corresponding Prony series (Table 1), which were implemented into the FEA. Fig.1(b) shows that the experimental data and fitting curve agree well with each other. A sharp decrease of the modulus is observed at the beginning and the steady state is reached in 1200s. As a result, the initial modulus, which is the sum of all moduli of the springs, is 0.96068 MPa, while the long-term modulus is 0.81988 MPa. The relaxation has accomplished by 99.40% at t=1200 s. On the other hand, to determine the true primary relaxation time, free fitting without any limitation of timescales was also implemented using two terms of Prony Series, resulting in  $\tau'_1 = 3.7079$ ,  $\tau'_2 = 67.9024$ ,  $g'_1 = 0.0583$ ,  $g'_2 = 0.0322$ ,  $E'_0 = 0.91079$ , but with an error of 94.8%. The primary relaxation time  $\tau'_1$  will be used for normalization later.

Table 1 Fitting results of the viscoelastic parameters for Sylgard 184 with a base-to-crosslinker ratio 15:1

Parameters	$E_0$ /MPa	n	$g_1 \\ (\tau_1 = 0.3/s)$	$g_2  (\tau_2 = 3/s)$	$g_3  (\tau_3 = 30/s)$	$g_4 \\ (\tau_4 = 300/s)$	$g_5 = (\tau_5 = 500/s)$
Values	0.96068	5	0.05069	0.04782	0.02967	0.01227	0.00671

# 2.3 Fabrication of imperfect viscoelastic domes

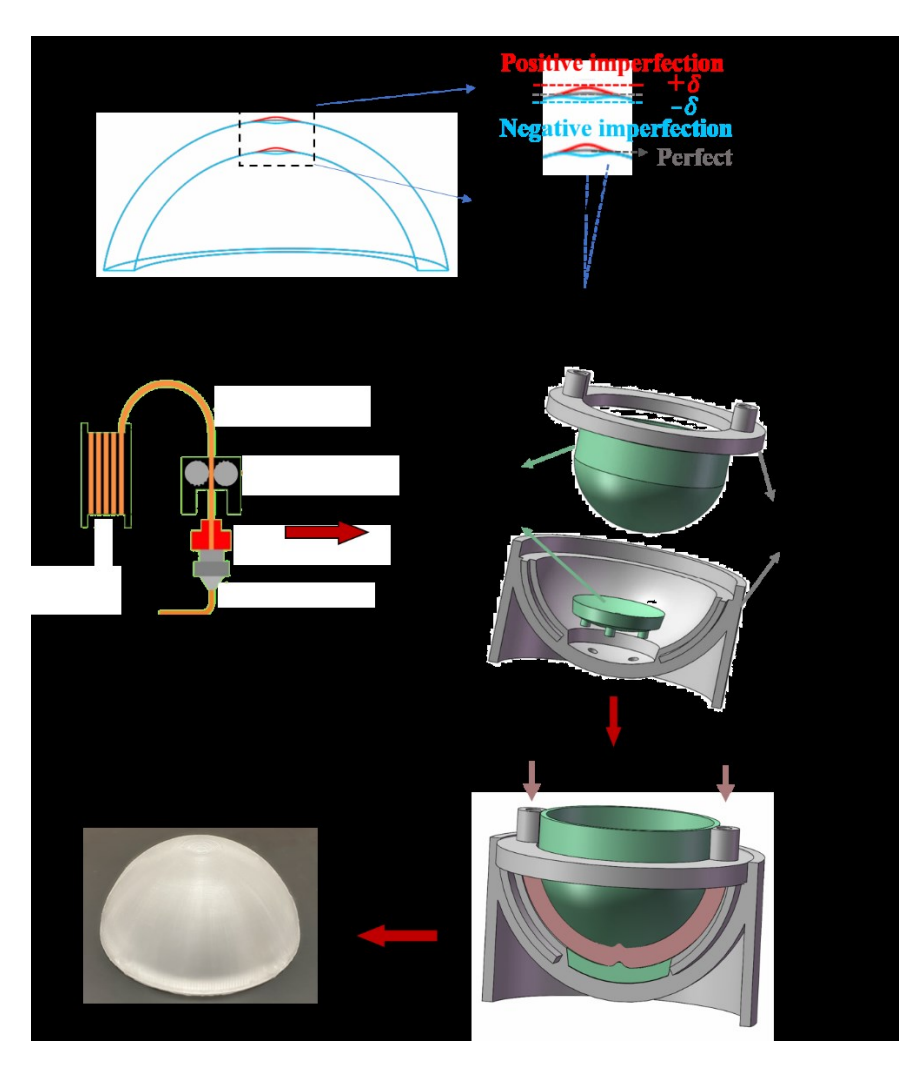


Fig.2. (a) A spherical dome with a Gaussian dimple imperfection including a positive amplitude marked in red or a negative amplitude marked in blue. (b) Fabrication process of a viscoelastic spherical dome with a predesigned imperfection. First, 3D printing was employed to manufacture the PLA molds including two universal frames and two replaceable imperfection parts, which made it effective to vary the imperfection by only fabricating the replaceable parts. Then Sylgard 184 was infused into the mold, followed by being cured for 24 h. Finally, the viscoelastic dome with a geometric imperfection was demolded.

To experimentally validate the geometric role of imperfections on the pseudo-bistability of viscoelastic domes and compare with the FEA results, we fabricated viscoelastic domes by mold casting using Sylgard 184. The molds made of polylactic acid (PLA) were manufactured by fused deposition modeling (FDM) 3D printing (Ultimaker S5 Printer). Each mold was assembled by four parts: two universal frames and two replaceable imperfection parts (Fig.2b); therefore, to vary the imperfection for a dome with given geometry, only the imperfection parts need to be fabricated and replaced. A Sylgard 184 prepolymer solution with a base-to-crosslinker ratio 15:1, was vacuumed until no trapped bubbles, followed by being poured into the printed PLA mold. Degassing was run for a second time to eliminate air bubbles that may be introduced during the infusion process. Then the mixture was cured for 24 h at room temperature. Finally, the viscoelastic dome sample with a predesigned geometric imperfection was obtained after demolding.

#### 2.4 Indentation tests

Indentation tests were performed on a viscoelastic dome using an Instron testing machine with a custom-mounted indenter (Fig.1c). The indenter was manufactured by FDM 3D printing using PLA with a 90% infill density, which is expected to minimize deformation of the indenter during loading due to its high stiffness compared to that of the dome. An acrylic platform with a hole in the center served as the base to support the dome and was lubricated by oil applied on the contact surface to minimize friction. Note that even with the lubrication, the friction could not be eliminated completely. Moreover, the platform could only provide restriction to downward vertical displacement. Therefore, the boundary conditions in the experiments and FEA are slightly different. The loading procedure is the same as that in FEA: a displacement was applied to the dome by the indenter with a loading rate of 20 mm/min; the indenter was kept at the deformed position to allow the material to relax after loading; then the indenter was removed, followed by recovery of the dome to its original shape after a certain amount of time. The load-displacement relations and recovery time were recorded during the testing.

# 3. Stability of perfect viscoelastic domes

The stability of perfect viscoelastic domes was characterized by both FEA and experiments. Depending on its geometric and material properties, a viscoelastic dome could show monotonicity, monostability, bistability or pseudo-bistability when it is indented to an inverted position and held for certain amount of time. Particularly, the geometry is crucial in determining whether the instantaneous response of the dome is monostable or bistable, while the evolution of the material properties during the relaxation  $(0-t_{rel})$  and

recovery  $(t > t_{rel})$  is the dominant factor in determining whether pseudo-bistable behavior occurs.

Here by varying the initial angle of a viscoelastic dome from 75°, 80.2° to 85°, but fixing the inner radius  $r_1 = 24.9$  mm and outer radius  $r_2 = 30.1$  mm, we show that the dome can be tuned from monostable, pseudo-bistable to bistable, as demonstrated by its instantaneous indentation forcedisplacement relation (Fig.3a, b), and the displacement-time relation in the relaxation and recovery processes (Fig.3c). The monotonic case, which is too far away from the region we are interested in, is shown in Supplementary information S1. The reaction force f is normalized by the initial modulus  $E_1 + E_{\infty}$ and the square of the width  $w_0^2$ ,  $f/(E_0 + E_{\infty})w_0^2$ , while the displacement v is normalized by  $w_0$ ,  $v/w_0$ . In all the three cases, both FEA and experimental results show that the normalized reaction force  $f/(E_0 + E_{\omega})w_0^2$  first increases until reaching a limit point, then decreases until reaching a second limit point, and increases again with the normalized displacement  $v/w_0$  (Fig.3a, b). When  $\alpha_0 = 75^{\circ}$  or 80.2°, the second limit point, i.e. the minimum reaction force, is positive (the blue or red curves in Fig. 3a, b), corresponding to instantaneously monostable behavior. However, the dome with  $\alpha_0 = 80.2^{\circ}$  has a minimum reaction force very close to zero, indicating its geometric parameters are close to the boundary between the monostable and bistable behavior. When  $\alpha_0 = 85^{\circ}$ , the minimum reaction force is negative (the black curve in Fig. 3a, b), corresponding to instantaneously bistable behavior. The FEA (Fig. 3a) and experimental results (Fig. 3b) show good agreement. The slight discrepancy of both the limit points between the FEA and experiments is attributed to the difference between the boundary conditions, and the friction between the base of the domes and the acrylic platform leads to higher reaction forces in the experiments.

After an indentation displacement of 2H is held for t = 10 s ( $t/\tau_1 = 2.70$ ,  $\tau_1 = 3.7079$  the primary relaxation time scale), it is released, and the displacement-time relations of the domes are recorded in Fig. 3c. The dome with an initial angle  $\alpha_0 = 75^{\circ}$  recovers the original shape without much delay once the indentation is released (blue curves in Fig. 3c), indicating monostability. The dome with  $\alpha_0 = 80.2^{\circ}$  remains almost stationary for the normalized snap time  $t_{snap}/\tau_1' = 16.18$  in the FEA and for  $t_{snap}/\tau_1' = 10.79$  in the experiment before sudden recovery (red curves in Fig. 3c). This behavior indicates pseudo-bistability of the dome, with the feature that the minimum reaction force is greater than 0 in the instantaneous deformed state, but the dome becomes bistable after viscoelastic relaxation under the indentation, while eventually becomes monostable again due to the viscoelastic relaxation after the indenter is released. The bistable case is demonstrated by the dome with an initial angle 85° (black curves), which possesses a negative minimum force (Fig. 3a, b), and keeps stable in the inverted configuration (Fig. 3c). The FEA and experimental results agree reasonably well with each other (Fig. 3c).

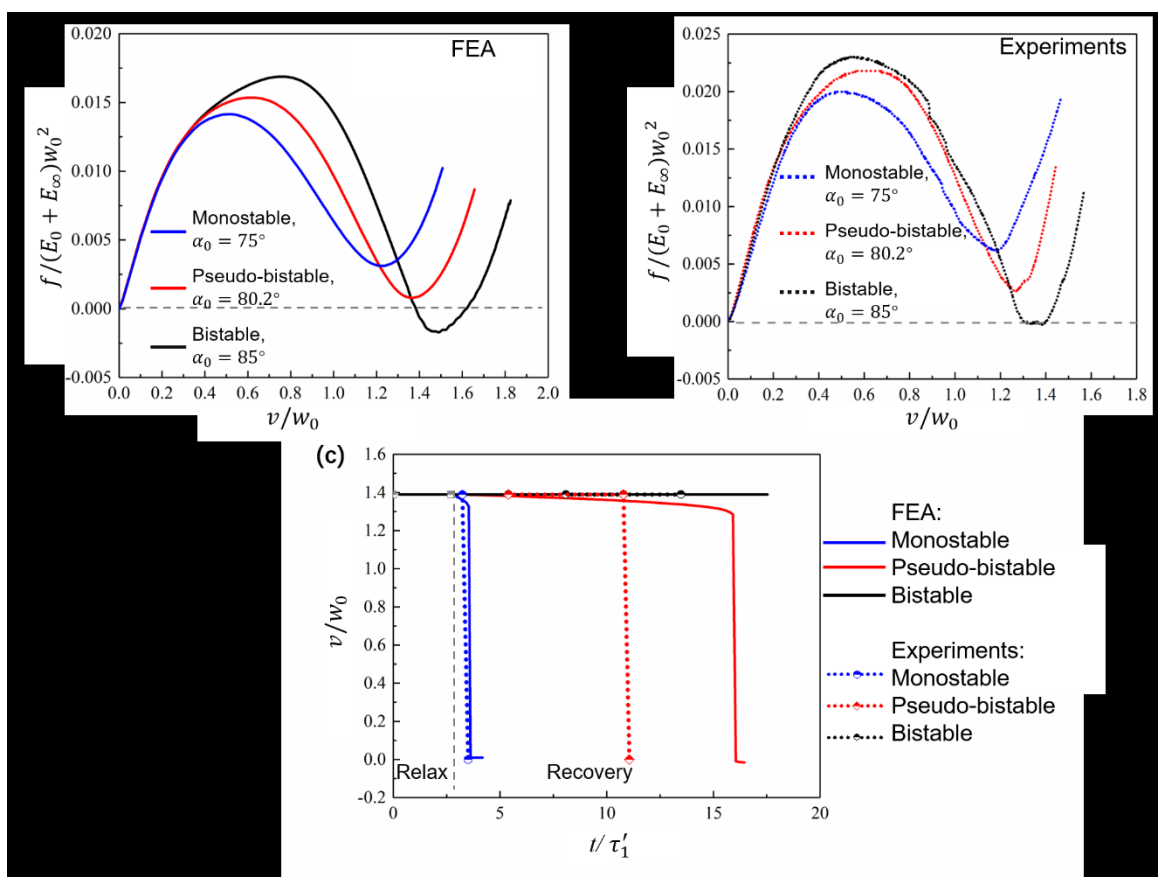


Fig.3. (a)-(b) Normalized force and displacement relations of perfect viscoelastic domes with the initial angle  $\alpha_0 = 75^{\circ}$ , 80.2°, 85° in the deformation step from (a) FEA and (b) experiments show monostability, pseudo-bistability bistability, respectively. (c) Displacements and time relations in the relaxation and recovery processes from FEA (solid lines) and experiments (dashed lines).

# 4. The effect of geometric imperfections on pseudo-bistability

In this section, we conduct FEA and experiments to demonstrate the effect of imperfections on pseudo-bistability of viscoelastic domes. Using the dome with an initial angle  $\alpha_0 = 80.2^{\circ}$  discussed in Sec 3 as a typical example of pseudo-bistable behavior, we introduce Gaussian dimple imperfections with various amplitudes and widths into the dome. Specifically, the amplitude  $\delta$  is varied from -0.6h to 0.2h such that both negative and positive imperfections are considered, while the decay width of the polar angle,  $\beta_I$ , changes from 2.68° to 8.04° (Fig. 4). The normalized force-displacement relations of the imperfect viscoelastic domes in the instantaneous deformation step are compared with those of the perfect domes (FEA in Fig.4a, and experiments in Fig.4b). Both the FEA and experiments show that for the given geometry of the dome and indenter, both the limit points increase with the amplitude of the imperfection. We find that although the effect of imperfections on the maximum reactive force can be sensitive to both the geometry

of the dome and indenter, the results of the effect of imperfections on the minimum reactive force are representative. Since the main focus of this work is the influence of imperfections on pseudo-bistability, we will mainly focus on the changes of the minimum reactive force due to imperfections. A negative imperfection increases the minimum reactive force, indicating that the imperfect dome moves towards monostable behavior, while a positive imperfection brings the minimum reactive force closer to zero, and therefore, closer to the boundary between the monostable and bistable behavior. On the other hand, under a constant imperfection amplitude ( $\delta$ =-0.5h), the minimum reactive force increases with the decay width of polar angle,  $\beta_I$ . Consequently, the normalized snap time  $t_{snap}/\tau'_1$  of the imperfect domes also deviates from that of the perfect one (Fig.4c). Consistent results obtained from FEA and experiments show that a positive imperfect increases the snap time, while a negative imperfection decreases the snap time. The change of the normalized snap time,  $\Delta t_{snap}/\tau'_1$ , increases with both the amplitude and decay width of the imperfection. However, the positive imperfections are more efficient in increasing  $t_{snap}/\tau'_1$  than the negative imperfections in decreasing  $t_{snap}/\tau'_1$ .

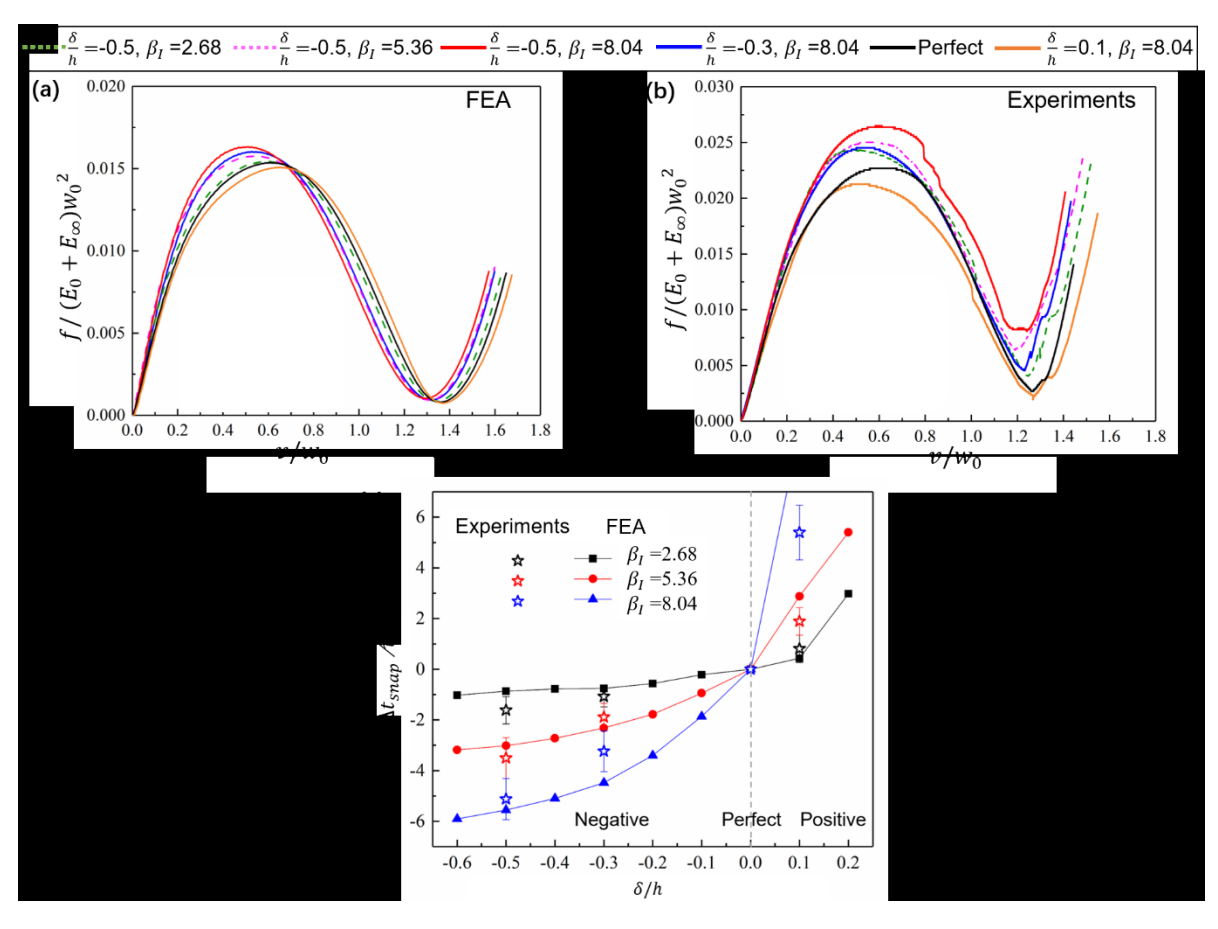


Fig.4. (a)-(b) Normalized force and displacement relations of viscoelastic domes with imperfections of various amplitudes and decay widths from (a) FEA and (b) experiments. The four solid lines show the effect of different amplitudes for a fixed width, while the two dashed lines and the red line show the effect of

different widths for a fixed amplitude. (c) The corresponding changes of the normalized snap time with respect to that of the perfect dome,  $\Delta t_{snap}/\tau_1'$ , from FEA (solid lines) and experiments (stars).

# 5. A discrete model for pseudo-bistability

In the literature, the phenomena of snap-through instability and pseudo-bistability of domes have been investigated by using discrete models to reveal the underlying mechanisms [8, 26, 27]. Here, a discrete model with an introduced geometric imperfection is developed to understand the effects of imperfections on pseudo-bistability observed in the FEA and experiments, and to predict the imperfection sensitivity of viscoelastic domes. In this section, perfect viscoelastic systems are first studied to show their instantaneous responses and dynamic behaviors. Then the roles that geometric imperfections play in stability, snapping time and critical relaxation time are illuminated.

Following the literature [8], we simplify a viscoelastic dome by a discrete model consisting of a point mass, a vertical SLS material unit, and two tilted springs (Fig.5a). It is worth mentioning that the model in the literature [8] was used for an arch structure, whose difference from a dome is lack of a geometric constraint in the hoop direction. Since here we only consider axisymmetric deformation of domes, the deformation in both the radial and hoop directions, and therefore the corresponding energy terms, can be completely determined by the one-dimensional distributions of deflection and rotation of a dome, similar to that of an arch. Consequently, the effect of adding the energy caused by hoop deformation is equivalent to changing the effective stiffness of the vertical and tilted springs in the discrete model. Therefore, here we can still use it to study domes. Recall that the SLS model is degenerated from the generalized Maxwell-Wiechert model when n=1, and it can describe both relaxation and creep with the minimum number of Maxwell elements. It is assumed that the mass is jointed to one end of the viscoelastic unit and one end of the tilted spring, while the other end of the tilted spring is connected with the base by a pin joint. When a vertical downward displacement v is applied to the mass, the base would rotate around the pin joint. As the displacement increases, the energy of the vertical springs in the viscoelastic unit increases monotonically, representing the bending effect of a dome. In contrast, the energy of the tilted springs increases to the maximum value when they are horizontal, and then starts to decrease, which corresponds to the stretching effect of the dome. It is commonly recognized that it is the relative change between the bending and stretching energy caused by viscoelasticity that can trigger the transition between different stability states and drive the pseudo-bistable phenomenon. Therefore, introducing viscoelasticity only to the bending part here is enough to capture this behavior.

The geometric imperfections are described as deviations of the mass from its perfect location by amplitude  $\delta$  and width  $w_1$  (Fig.5a). Consequently, each tilted spring is divided into two parts including

the imperfect part with the defect and the perfect part. The stiffness of the tilted springs, the free linear spring in the viscoelastic unit, and the spring in the Maxwell element are denoted by  $k_{1s}$ ,  $k_{2s}$ ,  $k_{\infty}$  and  $k_1$ , respectively, and the viscosity of the dashpot is denoted by  $\eta$ . Therefore, the initial stiffness of the viscoelastic unit without relaxation is  $k_1 + k_{\infty}$ , while the long-term stiffness after full relaxation decays to  $k_{\infty}$ . For the perfect system, the stiffness of the tilted spring is denoted by  $k_s$ , and the width and inclination angle of the tilted spring are  $w_0$  and  $\alpha_0$ , respectively. The inclination angle of the imperfect spring is denoted as  $\alpha$ .

#### 5.1 Pseudo-bistability of a perfect system

#### 5.1.1 Instantaneous force-displacement responses

In this section, the instantaneous force-displacement responses of perfect viscoelastic systems are first explored. The dome is suddenly loaded by a downward displacement v at the mass point m, and the corresponding reaction force f is calculated. Consequently, the change in the length of each tilted elastic spring  $\Delta l$  can be approximately written as [8]

$$\Delta l \approx \frac{v}{2w_0} \left( v - 2\alpha_0 w_0 \right),\tag{4}$$

under the assumption that  $\alpha_0$  is small. The exact expression of  $\Delta l$  and the corresponding results are presented in Supplementary information S2. As we will see later that the approximate formula gives us a similar trend in predicting the force-displacement responses of the discrete viscoelastic system (Fig.5b and Fig.S2). Therefore, to provide more straightforward understanding, the approximate formula under the assumption of small  $\alpha_0$  is shown in the main text. It should be noted that the exact expression of  $\Delta l$  should be used for very deep domes. Since the instantaneous modulus of the SLS unit is  $k_{\infty} + k_1$ , the total energy of the SLS unit completely stored in its springs is  $\frac{1}{2}(k_{\infty} + k_1)v^2$ , and the potential energy of the system can be expressed as:

$$\Pi(v) = \frac{1}{2} (k_1 + k_{\infty}) v^2 + k_s \Delta l^2 - f v.$$
 (5)

The equilibrium states can be obtained by minimizing the potential energy with respect to v

$$\frac{\partial \Pi}{\partial v} = (k_1 + k_{\infty})v + \frac{k_s}{w_0^2}v(v - 2\alpha_0 w_0)(v - \alpha_0 w_0) - f = 0,$$
(6)

which leads to

$$f = (k_1 + k_{\infty})v + \frac{k_s}{w_0^2}v(v - 2\alpha_0 w_0)(v - \alpha_0 w_0).$$
 (7)

We can normalize the equation as

$$F = K_r V + \alpha_0^2 V(V - 2)(V - 1), \tag{8}$$

with

$$F = \frac{f}{k_s w_0 \alpha_0}, \ V = \frac{v}{w_0 \alpha_0}, \ K_r = \frac{k_1 + k_\infty}{k_s},$$
 (9)

where  $K_r$  is the relative stiffness of the vertical SLS unit compared to the tilted elastic springs, representing the stiffness ratio of bending to stretching. The normalized instantaneous force-displacement behavior only depends on  $\alpha_0$  and  $K_r$ .

Under different material and geometric parameters, the system shows different stability, which has also been observed in the literature [8]. Given a fixed inclination angle  $\alpha_0 = 0.8$ , the force-displacement curves for various  $K_r$  are shown in Fig. 5b. When  $K_r = 0.7$ , the force-displacement relation is monotonically increasing. When  $K_r = 0.3$ , the force-displacement relation becomes non-monotonic, although the second limit point is still higher than zero, indicating monostable behavior. When  $K_r$  is reduced to 0.16, the second limit point reaches zero, representing the transition from the monostable to bistable state. Bistable behavior is observed when  $K_r = 0.1$  with the second limit point lower than zero, yielding two additional intersection points with the x axis besides the origin.

To construct a phase diagram for the different stability behaviors with respect to  $\alpha_0$  and  $K_r$ , we determine the number of limit points and the value of the second limit point by finding the roots of the equation  $\partial F/\partial V = 0$ . The condition that there exist two limit points yields

$$K_r - \alpha_0^2 < 0. {10}$$

Whether the system is monostable or bistable is further determined by the force value at the second limit point  $V_2$ ,

$$F_{\min} = F(V = V_2) = K_r \left(1 + \sqrt{\frac{1}{3} - \frac{K_r}{3\alpha_0^2}}\right) - \alpha_0^2 \left(\frac{2}{3} + \frac{K_r}{3\alpha_0^2}\right) \sqrt{\frac{1}{3} - \frac{K_r}{3\alpha_0^2}}.$$
 (11)

When  $F_{min} > 0$ , the system is monostable, and the dome recovers the initial state whenever it is unloaded. When  $F_{min} < 0$ , the system is bistable. In particular, the equilibrium is stable when  $0 < V < V_1$  or  $V > V_2$   $V_2$ , and unstable under the condition of  $V_1 < V < V_2$ , with  $V_1$  the first limit point. Based on the above criteria, a phase diagram composed of the monotonic, monostable and bistable regions with respect to  $\alpha_0$  and  $K_r$  is plotted in Fig.5c. As a result, when  $\alpha_0$  is large and  $K_r$  is small the system is bistable. Decreasing  $\alpha_0$  or increasing  $K_r$  brings the system to the monostable region, until eventually the two limit points disappear, when the system becomes monotonic.

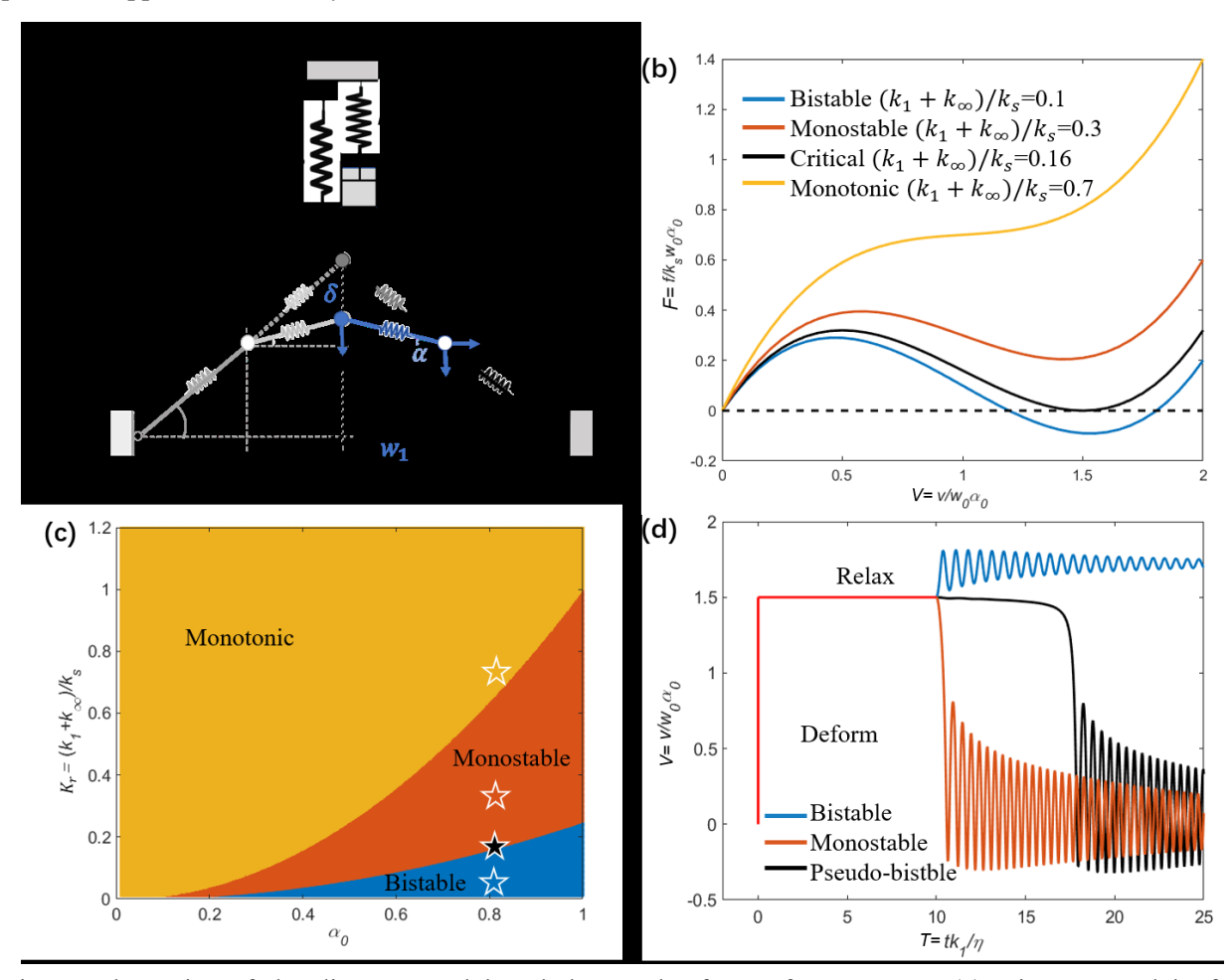


Fig.5. Schematics of the discrete model and the results for perfect systems. (a) Discrete model of a viscoelastic dome with a predesigned geometric imperfection, including a point mass, a viscoelastic unit, and two tilted springs with each divided into an imperfect and a perfect part. (b) Representative force-displacement responses showing bistable ( $\alpha_0 = 0.8, K_r = 0.1$ ), monostable ( $\alpha_0 = 0.8, K_r = 0.3$ ), monotonic ( $\alpha_0 = 0.8, K_r = 0.7$ ) and critical behavior on the boundary between bistable and monostable states ( $\alpha_0 = 0.8, K_r = 0.16$ ). (c) Phase diagram of monotonic, monostable, and bistable behaviors with respect to  $\alpha_0$  and  $K_r$ , where the stars represent the parameters used for the force-displacement curves in b. (d) Trajectories of the mass as functions of time for a monostable system ( $K_r = 0.3840$ ), bistable system ( $K_r = 0.2560$ ) and pseudo-bistable system ( $K_r = 0.3206$ ) under an instantaneous normalized displacement loading  $V_1 = 1.5$ , relaxation for  $T_{rel} = 10$ , and recovery, with the other parameters fixed as  $\widetilde{K} = 0.5$ ,  $\alpha_0 = 0.8$  and  $T_r = 0.01$ .

#### 5.1.2 Dynamic pseudo-bistability behaviors

Next, the dynamics of the perfect system in the different stability regions is investigated to especially unravel the pseudo-bistability behavior. Recall that a sudden downward displacement is applied to the mass m at t=0, which is kept constant during the time period of 0- $t_{rel}$ . At  $t=t_{rel}$ , the external force f is removed to release the mass. The relation between the total force  $f_b$  applied to the viscoelastic unit and the displacement v can be expressed as

$$\frac{k_1 + k_\infty}{k_1} \frac{dv}{dt} + \frac{k_\infty}{\eta} v = \frac{1}{k_1} \frac{df_b}{dt} + \frac{1}{\eta} f_b. \tag{12}$$

Accounting for the downward indentation force *f*, and the forces from the vertical viscoelastic unit and tilted springs, the conservation of momentum of the mass is described as

$$m\frac{d^2v}{dt^2} = \frac{k_s v}{w_0^2} (v - 2\alpha_0 w_0)(\alpha_0 w_0 - v) - f_b + f, \qquad (13)$$

where the first term on the right hand side of Eq. (13) represents the force from the tilted springs obtained in Eq. (7). Eq. (12) and Eq. (13) can be normalized as the following

$$K_r \frac{dV}{dT} + (1 - \tilde{l}) \qquad \frac{lF_b}{dT} + F_b \,, \tag{14}$$

$$T_r \frac{d^2 V}{dT^2} = \alpha_0^2 V(V - 2)(1 - V) - F_b + F, \qquad (15)$$

where

$$T = \frac{k_1 t}{\eta}, \ F_b = \frac{f_b}{k_s w_0 \alpha_0}, \ T_r = \frac{m k_1^2}{k_s \eta^2}, \ \tilde{I} \qquad \kappa_1 + \kappa_{\infty}$$
 (16)

besides the dimensionless variables and parameters defined in Eq. (8). The dimensionless parameter  $\widetilde{K}$  represents the degree of relaxation of the viscoelastic unit. Time t is normalized by the viscoelastic time scale  $\eta/k_1$ , and the dimensionless parameter  $T_r$  indicates the square of the time scale ratio of the period of resonance  $\sqrt{m/k_s}$  to viscoelasticity  $\eta/k_1$ .

In the relaxation step, the external force evolves as a result of the stress relaxation in the viscoelastic part, while the displacement  $V_0$  applied suddenly in the deformation step remains a constant. The external force F as a function of time is entirely determined by  $V_0$  and the effective stiffness of the viscoelastic unit, which evolves with time  $K_r^{eff}(T)$ ,  $F(T) = F(V_0, K_r^{eff}(T))$ . Solving the effective stiffness  $K_r^{eff}(T)$  using Eq. (14) by prescribing the step displacement  $V_0H(t)$ , and plugging  $F_b$  back to Eq. (15) yield

$$F(T) = V_0 K_r^{eff}(T) + \alpha_0^2 V_0 (V_0 - 2)(V_0 - 1),$$

$$K_r^{eff}(T) = K_r (1 - \tilde{I})$$
(17)

Then we can get the expression of the external force for the entire process by describing it with the Heaviside step function as  $F = F[1 - H(T - T_{rel})]$ . In the release step, the external force is 0, and we can determine the evolution of V by solving the coupled Eqs. (14) and (15) using the command ode45 in MATLAB with the following initial conditions of V,  $\dot{V}$  and  $F_b$  at  $T = T_{rel}$ 

$$V = V_0, \ \mathcal{V} = K_r^{eff}(T_{rel})V_0.$$
 (18)

By prescribing the parameters  $\tilde{K}=0.5$ ,  $\alpha_0=0.8$ ,  $T_r=0.01$ ,  $V_0=1.5$ , and varying  $K_r$ , we show the typical dynamic behaviors of the system in Fig.5d, including the monostable, bistable and pseudo-bistable behaviors. After being applied an instantaneous displacement  $V_0$ , the mass is held for a certain amount of time  $T_{rel}=t_{rel}k_1/\eta=10$  before being released. When  $K_r=0.3840$ , the system is monostable, rapidly recovers its initial state, and vibrates around it once the load is released. As the relative stiffness  $K_r$  decreases, the system becomes bistable. Once the indenter is released, the bistable system with  $K_r=0.2560$  snaps to the inverted state, instead of the initial state. However, when  $K_r=0.3206$ , the response of the system after the indenter is released is considerably slowed down. The mass remains at an almost constant position for a few times of the viscoelastic relaxation time, until it rapidly accelerates, snaps back to the initial sate, which is the pseudo-bistable behavior, and vibrates around the initial state. Note that no vibration is observed in the FEA, since numerical damping is applied. We will next use the discrete mode to investigate the effect of geometric imperfections on the pseudo-bistability.

# 5.2 Imperfection-sensitivity of pseudo-bistability

We present here the role of geometric imperfections in changing the pseudo-bistable behavior and the imperfection-sensitivity of dynamic behavior and critical relaxation time, which refers to the minimum relaxation time required for a structure to show pseudo-bistability. The results from the discrete model will be used to qualitatively compared with and explain the observations from the FEA and experiments.

A deviation of the mass from its perfect position by a small amplitude  $\delta$  and width  $w_1$  is introduced, consequently altering the inclination angle of imperfect part from  $\alpha_0$  to  $\alpha$ 

$$\frac{\delta}{w_1} = \tan \alpha - \tan \alpha_0 \approx \alpha - \alpha_0. \tag{19}$$

The tilted spring is divided into two parts by the imperfection, which are imperfect part with stiffness  $k_{1s}$  and width  $w_1$ , and perfect part with stiffness  $k_{2s}$  and width  $w_2$ . The displacements of the connected point

in vertical and horizontal direction are denoted as  $v_2$  and  $u_2$ . When the dome is loaded by a downward displacement  $v_1$  at the mass point, the changes in the lengths of the two tilted parts can be approximately written as

$$\Delta l_1 \approx \frac{1}{2w_1} (u_2^2 + (v_1 - v_2)^2 + 2u_2w_1 - 2\alpha w_1(v_1 - v_2)),$$

$$\Delta l_2 \approx \frac{1}{2w_2} (u_2^2 + v_2^2 - 2u_2w_2 - 2\alpha_0 w_2 v_2).$$
(20)

So, the potential energy of the system can be expressed as:

$$\Pi(v) = \frac{1}{2} (k_1 + k_{\infty}) v_1^2 + k_{1s} \Delta l_1^2 + k_{2s} \Delta l_2^2 - f v_1.$$
 (21)

The equilibrium states can be obtained by minimizing the potential energy with respect to the displacements

$$\frac{\partial \Pi}{\partial v_{1}} = (k_{1} + k_{\infty})v_{1} + 2k_{1s}\Delta l_{1} \frac{\partial \Delta l_{1}}{\partial v_{1}} - f = 0,$$

$$\frac{\partial \Pi}{\partial u_{2}} = 2k_{2s}\Delta l_{2} \frac{\partial \Delta l_{2}}{\partial u_{2}} + 2k_{1s}\Delta l_{1} \frac{\partial \Delta l_{1}}{\partial u_{2}} = 0,$$

$$\frac{\partial \Pi}{\partial v_{2}} = 2k_{2s}\Delta l_{2} \frac{\partial \Delta l_{2}}{\partial v_{2}} + 2k_{1s}\Delta l_{1} \frac{\partial \Delta l_{1}}{\partial v_{2}} = 0.$$
(22)

It is assumed that the stiffness of imperfect and perfect parts satisfies

$$\frac{k_{2s}}{k_{1s}} = \frac{w_1}{w_2}, \frac{1}{k_{1s}} + \frac{1}{k_{2s}} = \frac{1}{k_s}.$$
 (23)

Then the equilibrium Eqs. (22) can be derived as

$$f = (k_{1} + k_{\infty})v_{1} + k_{s} \frac{w_{1} + w_{2}}{w_{1}} \frac{v_{1} - v_{2} - \alpha w_{1}}{w_{1}^{2}} (u_{2}^{2} + (v_{1} - v_{2})^{2} + 2u_{2}w_{1} - 2\alpha w_{1}(v_{1} - v_{2})),$$

$$\frac{u_{2} - w_{2}}{w_{2}^{3}} (u_{2}^{2} + v_{2}^{2} - 2u_{2}w_{2} - 2\alpha_{0}w_{2}v_{2}) + \frac{u_{2} + w_{1}}{w_{1}^{3}} (u_{2}^{2} + (v_{1} - v_{2})^{2} + 2u_{2}w_{1} - 2\alpha w_{1}(v_{1} - v_{2})) = 0,$$

$$\frac{v_{2} - \alpha_{0}w_{2}}{w_{2}^{3}} (u_{2}^{2} + v_{2}^{2} - 2u_{2}w_{2} - 2\alpha_{0}w_{2}v_{2}) - \frac{v_{1} - v_{2} - \alpha w_{1}}{w_{1}^{3}} (u_{2}^{2} + (v_{1} - v_{2})^{2} + 2u_{2}w_{1} - 2\alpha w_{1}(v_{1} - v_{2})) = 0.$$

$$(24)$$

We can normalize the equations as

$$F = K_{r}V_{1} + \frac{\alpha_{0}^{2}}{W_{1}^{3}}(V_{1} - V_{2} - \frac{\alpha}{\alpha_{0}}W_{1})(U_{2}^{2} + (V_{1} - V_{2})^{2} + 2U_{2}\frac{W_{1}}{\alpha_{0}} - 2\frac{\alpha W_{1}}{\alpha_{0}}(V_{1} - V_{2})),$$

$$\frac{U_{2} - \frac{W_{2}}{\alpha_{0}}}{W_{2}^{3}}(U_{2}^{2} + V_{2}^{2} - 2U_{2}\frac{W_{2}}{\alpha_{0}} - 2W_{2}V_{2}) + \frac{U_{2} + \frac{W_{1}}{\alpha_{0}}}{W_{1}^{3}}(U_{2}^{2} + (V_{1} - V_{2})^{2} + 2U_{2}\frac{W_{1}}{\alpha_{0}} - 2\frac{\alpha}{\alpha_{0}}W_{1}(V_{1} - V_{2})) = 0,$$

$$\frac{V_{2} - W_{2}}{W_{2}^{3}}(U_{2}^{2} + V_{2}^{2} - 2U_{2}\frac{W_{2}}{\alpha_{0}} - 2W_{2}V_{2}) - \frac{V_{1} - V_{2} - \frac{\alpha W_{1}}{\alpha_{0}}}{W_{1}^{3}}(U_{2}^{2} + (V_{1} - V_{2})^{2} + 2U_{2}\frac{W_{1}}{\alpha_{0}} - 2\frac{\alpha}{\alpha_{0}}W_{1}(V_{1} - V_{2})) = 0,$$

$$(25)$$

with

$$(V_1, V_2, U_2) = \frac{1}{w_0 \alpha_0} (v_1, v_2, u_2), \ W_1 = \frac{w_1}{w_0}, W_2 = \frac{w_2}{w_0},$$
(26)

besides the dimensionless variables and parameters defined in Eq. (8).

We plot the instantaneous force-displacement relations for the system with a small imperfection of various amplitudes  $\delta = -0.06w_0$ ,  $-0.02w_0$ ,  $0.02w_0$  and  $0.06w_0$  and width  $w_1 = w_0$  to compare with that of the perfect system (Fig.6a). Please note that here the imperfection amplitude is scaled by the width of the dome,  $w_0$ , instead of the thickness, since  $w_0$  is the only length scale in the discrete model. If we convert  $\delta/h$  in the experiments and FEA to  $\delta/w_0$  using the prescribed  $h/w_0$ , and compare the results with those of the discrete model, we can see that the amplitudes are on the same order of magnitude, which means we are using similar defect sizes. The perfect system with the parameters  $\tilde{K}=0.5$ ,  $\alpha_0=0.8$  and  $K_r$ =0.1626 is monostable, but is near the boundary between the monostable and bistable behavior. A negative imperfection decreases the maximum force, while increases the minimum force (Fig. 6b). On the other hand, a positive imperfection increases the maximum force, while decreases the minimum force. This means a negative imperfection pushes the system further deeper into the monostable region, while a positive imperfection pulls the system closer to the boundary, or even to transit to the bistable region when the minimum force is less than zero. The deviation from the perfect system increases as the amplitude of the imperfection increases. The results agree with the FEA and experiments. Therefore, a geometric imperfection with a relatively small amplitude could result in significant variations of the mechanical responses of domes, and can even be harnessed to program stability. When the width of the imperfection  $w_1$  is smaller, the deviation of the force-displacement curve from the perfect one is smaller (Figs. S3 and S4); see Supplementary information S3 for more details.

The dynamic trajectories of the system same as the pseudo-bistable case in Fig. 5d ( $K_r$ =0.3206) but with both positive and negative imperfections ( $\delta = -0.02w_0 \sim 0.04w_0$ ,  $w_1 = w_0$ ) are plotted in Fig.6c. For a negative imperfection, the snap time is observed to decrease as the amplitude of the imperfection increases, until reaching around zero, which approaches the monostable behavior. The snap time drops sharply at small imperfection amplitudes, and reaches a plateau at large imperfection amplitudes (Fig. 6d). When a small positive imperfection is introduced, the snap time increases with the amplitude of the imperfection ( $\delta/w_0 = 5 * 10^{-4}$ , the cyan curve in Fig. 6c). However, when the amplitude of the imperfection is large enough, the system becomes bistable with an infinite snap time (Fig. 6d). The dynamic results match well

with the trend observed in the FEA and experiments that a negative defect shifts the system towards the monostable behavior while a positive defect shifts the system towards the bistable behavior in the instantaneous response. It is worth mentioning that the dependence of the variation of the snap time on the amplitude of the imperfection is not linear (Fig. 6d). Specifically, the snap time and stability can change significantly with the amplitude of the imperfection near the threshold of a pseudo-bistable state, while they only change slightly far away from the threshold. We see a small variation of geometry ( $\alpha_0$ =0.795) from the system ( $\alpha_0$ =0.8), which is close to the boundary between monostability and bistability, leads to visible difference of snap time in Fig.6d.

We now explore how an imperfection affects the critical relaxation time under various geometric and material parameters. Pseudo-bistable behavior would occur if the force at the second limit point  $F_{min}$  is instantaneously greater than 0 and less than 0 after a long-term relaxation, yielding

$$F_{\min}(K_r^{eff}(0), \alpha_0) > 0,$$

$$F_{\min}(K_r^{eff}(\infty), \alpha_0) < 0.$$
(27)

To determine the critical relaxation time  $T_{rel}^c$ , we replace  $K_r$  in Eq. (11) by  $K_r^{eff}(T_{rel}^c)$  and use the condition

$$F_{\min}(K_r^{eff}(T_{rel}^c), \alpha_0) = 0$$
 (28)

We then expect the system will become pseudo-bistable when the relaxation time is larger than the critical value  $T_{rel} > T_{rel}^c$ . Fig.6e shows the critical relaxation time changes with the relative stiffness  $K_r$  for different imperfection amplitudes and inclination angles. The region of negative relaxation time  $T_{rel}^c < 0$  means the system is instantaneously bistable. It is reasonable that  $T_{rel}^c$  increases with the relative stiffness, and decreases with the inclination angle, because larger relative stiffness or a smaller inclination angle shifts the system towards the monostable region (Fig.5b), corresponding to a longer relaxation time. Similarly, a negative imperfection increases  $T_{rel}^c$ , while a positive imperfection decreases  $T_{rel}^c$ , because a negative imperfection also shifts the system towards the monostable region.

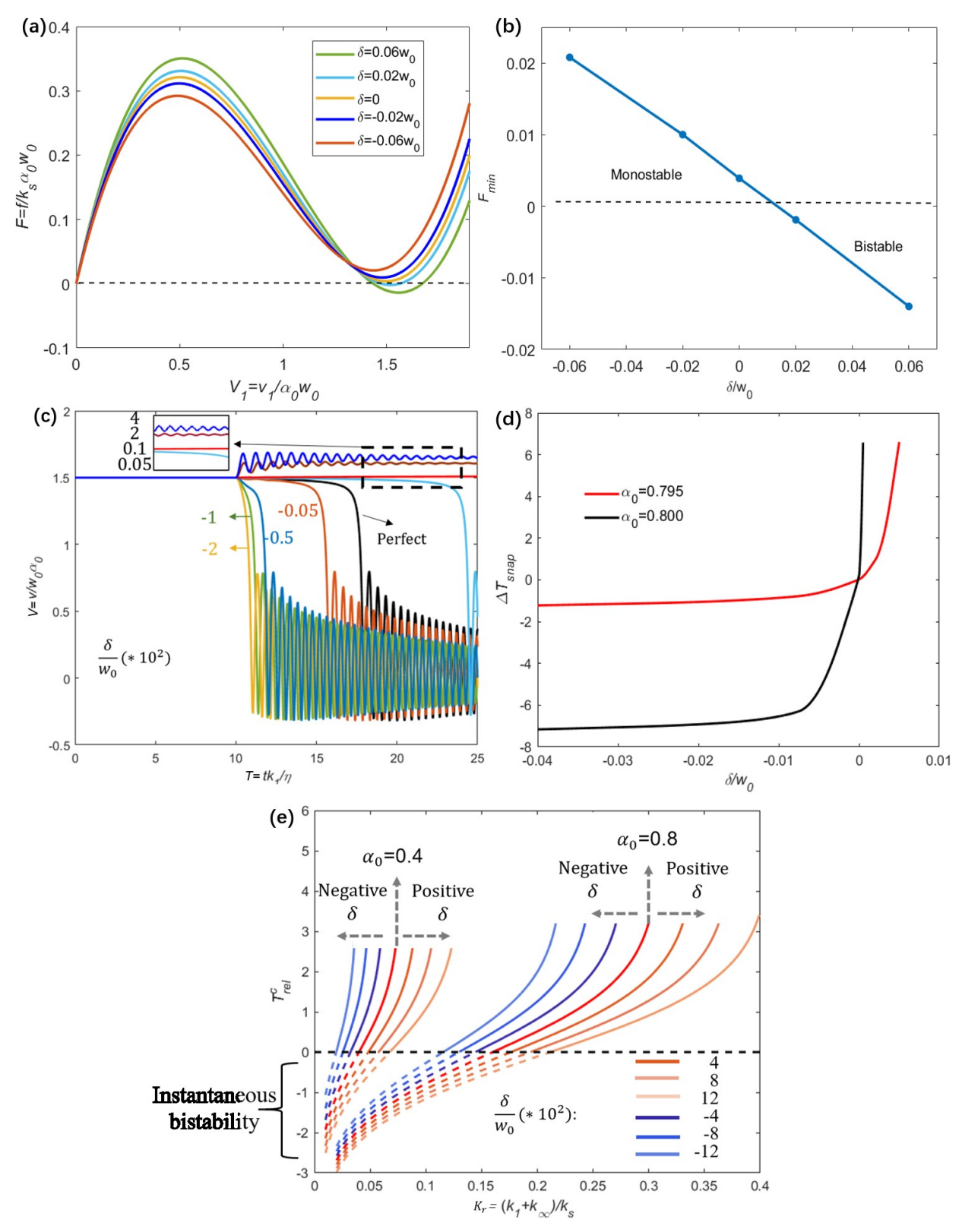


Fig.6. Results of the discrete model for imperfect systems. (a) Instantaneous force-displacement curves of the system with a predesigned geometric imperfection of a width  $w_1 = w_0$  and an amplitude varied from

-0.06 $w_0$  to 0.06 $w_0$ . (b) Dependence of the minimum force on the amplitude of the imperfection. (c) Dynamic responses of imperfect systems show a decrease of the snap time when the imperfection is negative, and an increase of the snap time when the imperfection is positive. (d) Snap time as a function of imperfection amplitude under different inclination angle  $\alpha_0$ . (e) The imperfection sensitivity of the critical relaxation time under various geometric and material parameters.

#### 6. Conclusions

In conclusion, this paper investigates the effect of geometric imperfections on pseudo-bistability of spherical viscoelastic domes by combining FEA, experiments, and analytical modeling. The amplitude and profile of imperfections are systematically varied and accurately controlled in both the FEA and experiments. Experimentally, perfect and imperfect silicone rubber domes are fabricated through 3D printed molds, and characterized for pseudo-bistable behavior with a loading procedure of deforming, holding and releasing by a custom-mounted indenter. The similar loading process is applied in FEA to examine the dynamic responses of both perfect and imperfect domes made of a generalized Maxwell-Wiechert material fitted to the relaxation test data. A discrete dynamic model of a viscoelastic dome is further developed to understand the geometric role of imperfections in the pseudo-bistable behavior. The results from the experiments, FEA, and discrete model agree well with each other, and show that a positive imperfection shifts a viscoelastic dome towards bistable behavior, corresponding to a longer snap time, while a negative imperfection shifts the dome towards monostable behavior, resulting in a shorter snap time. The discrete model unravels that the effect of an imperfection on snap time and stability is particularly strong when the system is near the threshold of a pseudo-bistable state. This work can motivate future exploration of the effect of imperfection shape and material properties on pseudo-bistability, and provide more opportunities for multi-functional designs [38-41]. It can also open up potential novel applications of viscoelastic domes by combining structural instability, geometric imperfections, especially with stimuli-responsive materials, whose material properties and geometry can change in response to external stimuli.

# Acknowledgements

This work is supported by the startup fund from Henry Samueli School of Engineering and Applied Science at the University of California, Los Angeles (UCLA), and National Science Foundation through a CAREER Award No. CMMI-2048219. This work used computational and storage services associated with the Hoffman2 Shared Cluster provided by UCLA Institute for Digital Research and Education's Research Technology Group. T.L. L.L. Y.L and J.L. acknowledge the National Natural Science Foundation of China (Grant Nos. 11632005, 11672086). T.L. acknowledges the support by China Scholarship Council (No. 201806120085). We also thank Dr. Jonathan Hopkins and Dr. Lucas A. Shaw at UCLA for providing us access to their Instron machine.

# Appendix A. Supplementary data

Supplementary material related to this article is provided.

# Reference

- [1] A. Cazzolli, F. Dal Corso, Snapping of elastic strips with controlled ends, International Journal of Solids and Structures 162 (2019) 285-303.
- [2] K. Che, M. Rouleau, J. Meaud, Temperature-tunable time-dependent snapping of viscoelastic metastructures with snap-through instabilities, Extreme Mechanics Letters 32 (2019) 100528.
- [3] L. Cedolin, Stability of structures: elastic, inelastic, fracture and damage theories, World Scientific 2010.
- [4] Y. Chen, L. Jin, Snapping-back buckling of wide hyperelastic columns, Extreme Mechanics Letters 34 (2019) 100600.
- [5] D. Chen, L. Jin, Controlled formation and disappearance of creases, Materials Horizons 1 (2014) 207-213.
- [6] F. Jia, M.B. Amar, Scaling laws and snap-through events in indentation of perforated membranes, Journal of the Mechanics and Physics of Solids 135 (2019) 103797.
- [7] Y. Forterre, J.M. Skotheim, J. Dumais, L. Mahadevan, How the Venus flytrap snaps, Nature 433(7024) (2005) 421.
- [8] M. Gomez, D.E. Moulton, D. Vella, Dynamics of viscoelastic snap-through, Journal of the Mechanics and Physics of Solids 124 (2019) 781-813.
- [9] A. Pandey, D.E. Moulton, D. Vella, D.P. Holmes, Dynamics of snapping beams and jumping poppers, EPL (Europhysics Letters) 105(2) (2014) 24001.
- [10] S. Shan, S.H. Kang, J.R. Raney, P. Wang, L. Fang, F. Candido, J.A. Lewis, K. Bertoldi, Multistable Architected Materials for Trapping Elastic Strain Energy, Advanced Materials 27(29) (2015) 4296-4301.
- [11] K. Che, C. Yuan, H.J. Qi, J. Meaud, Viscoelastic multistable architected materials with temperature-dependent snapping sequence, Soft matter 14(13) (2018) 2492-2499.
- [12] David, Restrepo, Nilesh, D, Mankame, Pablo, D, Zavattieri, Phase transforming cellular materials, Extreme Mechanics Letters 4 (2015) 52-60.
- [13] Z. Zhang, S. Pusateri, B. Xie, N. Hu, Tunable energy trapping through contact-induced snap-through buckling in strips with programmable imperfections, Extreme Mechanics Letters 37 (2020) 100732.
- [14] Y. Chen, L. Jin, Reusable Energy-Absorbing Architected Materials Harnessing Snapping-Back Buckling of Wide Hyperelastic Columns, Advanced Functional Materials (2021) 2102113.
- [15] M. Santer, Self-actuated snap back of viscoelastic pulsing structures, International Journal of Solids and Structures 47(24) (2010) 3263-3271.
- [16] C. Keplinger, T. Li, R. Baumgartner, Z. Suo, S. Bauer, Harnessing snap-through instability in soft dielectrics to achieve giant voltage-triggered deformation, Soft Matter 8 (2011) 285-288.
- [17] A. Arrieta, D. Wagg, S. Neild, Dynamic snap-through for morphing of bi-stable composite plates, Journal of Intelligent Material Systems and Structures 22(2) (2011) 103-112.
- [18] C. Bowen, R. Butler, R. Jervis, H. Kim, A. Salo, Morphing and shape control using unsymmetrical composites, Journal of Intelligent Material Systems and Structures 18(1) (2007) 89-98.

- [19] A. Carrella, F. Mattioni, A. Diaz, M. Friswell, D. Wagg, P. Weaver, Static and dynamic analysis of a bistable plate for application in morphing structures, 7th European Conference on Structural Dynamics, Southampton, 2008, pp. 7-9.
- [20] R.H. Plaut, Snap-through of arches and buckled beams under unilateral displacement control, International Journal of Solids and Structures 63 (2015) 109-113.
- [21] M. Taffetani, X. Jiang, D.P. Holmes, D. Vella, Static bistability of spherical caps, Proceedings of the Royal Society A: Mathematical, Physical Engineering Sciences 474(2213) (2018) 20170910.
- [22] A. Madhukar, D. Perlitz, M. Grigola, D. Gai, K.J. Hsia, Bistable characteristics of thick-walled axisymmetric domes, International Journal of Solids and Structures 51(14) (2014) 2590-2597.
- [23] N.C. Huang, W. Nachbar, Dynamic Snap-Through of Imperfect Viscoelastic Shallow Arches, Journal of Applied Mechanics 35(2) (1968) 289-296.
- [24] H.F. Brinson, L.C. Brinson, Polymer engineering science and viscoelasticity, Springer 2015.
- [25] R.S. Lakes, Viscoelastic solids, CRC press 1998.
- [26] A. Brinkmeyer, A. Pirrera, M. Santer, P. Weaver, Pseudo-bistable pre-stressed morphing composite panels, International Journal of Solids and Structures 50(7-8) (2013) 1033-1043.
- [27] A. Brinkmeyer, M. Santer, A. Pirrera, P. Weaver, Pseudo-bistable self-actuated domes for morphing applications, International Journal of Solids and Structures 49(9) (2012) 1077-1087.
- [28] E. Benet, H. Zhu, F.J. Vernerey, Interplay of elastic instabilities and viscoelasticity in the finite deformation of thin membranes, Physical review E 99(4) (2019) 042502.
- [29] E.Y. Urbach, E. Efrati, Predicting delayed instabilities in viscoelastic solids, Science Advances 6(36) (2020) eabb2948.
- [30] J.W. Hutchinson, E. Sciences, Buckling of spherical shells revisited, Proceedings of the Royal Society A: Mathematical, Physical 472(2195) (2016) 20160577.
- [31] C. Qiao, L. Liu, D. Pasini, Elastic thin shells with large axisymmetric imperfection: from bifurcation to snap-through buckling, Journal of the Mechanics Physics of Solids 141 (2020) 103959.
- [32] A. Lee, F. López Jiménez, J. Marthelot, J.W. Hutchinson, P.M. Reis, The Geometric Role of Precisely Engineered Imperfections on the Critical Buckling Load of Spherical Elastic Shells, Journal of Applied Mechanics 83(11) (2016) 111005.
- [33] C.D. Babcock, Shell Stability, Journal of Applied Mechanics 50(4b) (1983) 935-940.
- [34] J.W. Hutchinson, EML Webinar overview: New developments in shell stability, Extreme Mechanics Letters 39 (2020) 100805.
- [35] S. Gerasimidis, E. Virot, J.W. Hutchinson, S.M. Rubinstein, On Establishing Buckling Knockdowns for Imperfection-Sensitive Shell Structures, Journal of Applied Mechanics 85(9) (2018) 091010.
- [36] B. Budiansky, Theory of Buckling and Post-Buckling Behavior of Elastic Structures, 14 (1974).
- [37] F. Schneider, T. Fellner, J. Wilde, U. Wallrabe, Mechanical properties of silicones for MEMS, Journal of Micromechanics and Microengineering 18(6) (2008) 065008.
- [38] B. Gorissen, D. Melancon, N. Vasios, M. Torbati, K. Bertoldi, Inflatable soft jumper inspired by shell snapping, Science Robotics 5(42) (2020) eabb1967.
- [39] N. Vasios, B. Deng, B. Gorissen, K. Bertoldi, Universally bistable shells with nonzero Gaussian curvature for two-way transition waves, Nature Communications 12(695) (2021).
- [40] G. Wan, Y. Cai, Y. Liu, C. Jin, Z. Chen, Bistability in popper-like shells programmed by geometric defects, Extreme

Mechanics Letters 42 (2021) 101065.

[41] S. Janbaz, K. Narooei, T. van Manen, A.A. Zadpoor, Strain rate-dependent mechanical metamaterials, Science Advances 6(25) (2020) eaba0616.